# Tailoring Oxygen Reduction Reaction Pathway on Spinel Oxides via Surficial Geometrical-Site Occupation Modification Driven by Oxygen Evolution Reaction

*Li An,\* Yang Hu, Jianyi Li, Jiamin Zhu, Mingzi Sun, Bolong Huang,\* Pinxian Xi,\* Chun-Hua Yan*

Prof. L. An, Y. Hu, J. Li, J. Zhu, Prof. P. Xi

State Key Laboratory of Applied Organic Chemistry

Key Laboratory of Nonferrous Metal Chemistry and Resources Utilization of Gansu Province

Frontiers Science Center for Rare Isotopes

College of Chemistry and Chemical Engineering, Lanzhou University, Lanzhou, 730000, P. R. China.

E-mail: anli@lzu.edu.cn

E-mail: xipx@lzu.edu.cn

M. Sun, Prof. B. Huang

Department of Applied Biology and Chemical Technology

The Hong Kong Polytechnic University

Hong Hum, Kowloon, Hong Kong SAR (China)

E-mail: bhuang@polyu.edu.hk

Prof. C.-H. Yan

Beijing National Laboratory for Molecular Sciences

State Key Laboratory of Rare Earth Materials Chemistry and Applications

PKU-HKU Joint Laboratory in Rare Earth Materials and Bioinorganic Chemistry, Peking University

Beijing 100871 (China)

**Keywords:** partially inverse $MnCo_2O_4$, cations vacancies, geometrical-site occupation, surface reconstruction, oxygen reduction reaction

**Abstract:** Oxygen reduction reaction (ORR) has been demonstrated as a critical technology for both energy conversion technologies and hydrogen peroxide intermediate production. Herein, in-situ

oxygen evolution reaction (OER) surface evolution strategy is applied for changing the surface structure of $MnCo_2O_4$ oxide with tetrahedral and octahedral cations vacancies to realize reaction pathway switching from 2 $e^-$ ORR and 4 $e^-$ ORR. Interestingly, the as-synthesized $MnCo_2O_4$-pristine ($MnCo_2O_4$-P) with the highest surficial Mn/Co octahedron occupation favors two electrons reaction routes exhibiting high $H_2O_2$ selectivity ($\approx$ 80% and reaches nearly 100 % at 0.75 V vs. RHE); after surface atoms reconstruction, $MnCo_2O_4$-activation ($MnCo_2O_4$-A) with the largest Mn/Co tetrahedron occupation present excellent ORR performance through four electrons pathway with an ultrahigh onset potential and half-wave potential of 0.78 V and 0.92 V, ideal mass activity (MA) and the turnover frequencies (TOF) values. Density functional theory (DFT) calculations have revealed the concurrent modulations of both Co and Mn by the surface reconstructions, which improve the electroactivity of $MnCo_2O_4$-A towards the 4$e^-$ pathway. This work provides a new perspective to build correlation of OER activation-ORR property, bringing detailed understating for reaction route transformation, and thus guide the development of certain electrocatalysts with specific purposes.

## 1. Introduction

Oxygen reduction reaction (ORR) occurred at the cathode is critical for developing energy conversion technologies involving metal-air batteries and polymer electrolyte membrane fuel cells.[1] Electrochemical ORR has also been found as a green and safe route under ambient conditions to produce hydrogen peroxide intermediate ($H_2O_2$), which is one of the most valuable fundamental chemicals in various chemical industries, medical industries, and environmental remediation.[2] Interestingly, both these two focuses can be realized by the ORR process via different reaction routes or mechanisms. In detail, ORR with a complex multielectron process can proceed by two pathways, including the four-electron (4 $e^-$) or two-electron 2 $e^-$ ORR process to generate $H_2O$ or $H_2O_2$, respectively.[3] In the former pathway, oxygen is directly reduced to the final $OH^-$, which is usually facilitated by platinum (Pt)-based noble-metal electrocatalysts or some non-noble materials; while for the latter one, the firstly formed peroxide intermediates will either diffuse away from the disk electrode or continues to be reduced to form $OH^-$, which is commonly occurred on the surface of carbonaceous materials or transition-metal oxides.[4] As illustrated, the mechanism for ORR is strongly affected by the surface structure, coordination environment, really exposed active-centers, or crystal types of catalysts.[5] Among all the reported catalysts, typical mixed-metal cobalt

manganese oxides ($Mn_xCo_{3-x}O_{4\pm\delta}$, $0{\leq}x{\leq}3$, where $\delta$ indicates the oxygen non-stoichiometry) are usually deemed as promising catalysts in the oxygen electrochemical reaction, owing to high element abundance, considerable electro-activity, controllable tetrahedral and octahedral coordination, rich valence states.[6] Currently, various kinds of Mn-Co oxides have been reported for ORR; while, these oxides often exhibit large particle size or irregular shape, which affects their physicochemical properties and is the fatal drawback for superior catalytic performance. Moreover, the optional structural variations, multiple oxidation states, flexible structure, and elusive distribution of cations made the rational preparation process more complex. Therefore, it is feasible but difficult to synthesize Co-Mn oxides with controlled morphologies, homogenous phase, and alternated structural and chemical coordination for further ORR mechanism/pathway/route research.

Actually, compared with the bulk band, the catalyst's surface contacted with electrolyte is the real reaction place, and surficial structural/chemical evolution triggered by oxygen evolution reaction (OER) operation under high electric field has gained an increasing consensus for most electrocatalysts.[7] All these phenomena, such as phase transformation, component leaching, atom rearrangement, and so on could be deemed as inevitable surface change.[8] Additionally, surface structure engineering at the atomic level has been used as an efficient method to expose much more active sites for promoted electrocatalytic performance, demonstrating the importance of investigating the surficial structure-property relationship.[9] Typically, earlier efforts have successfully revealed that the oxygen electrocatalytic activity of perovskites is strongly related to the topmost surface (near-surface or evolved surface phase), while bears a little-to-no relationship to the structure of inner bulk itself.[10] These interesting findings have also been discovered on the spinel family on account of similar octahedral [$TMO_6$] (T means transition metals) sites as in perovskite oxides, which can be inspirations to further reveal the correlation between ORR performance and spinel oxides surficial structure.[6] In addition, the presence of tetrahedral [$TMO_4$] units in spinel oxide makes its electrocatalytic reaction and structure evolution more complicated.[11] Recently, some researchers have also exemplified that an intrinsic metal spinel-like surface can be found on the top layer of flexible perovskites, promoting the subsequent surface reconstruction. We thus believe that the structure of spinel oxides is much more sensitive than perovskites.[10] Therefore, using spinel oxides ($AB_2O_4$) as models, the ability to tune compositions and tetrahedron/octahedron occupation of A-sites and B-sites play a major role in the surface dynamical process. This has been realized by

many mature strategies, including defective modulation, atom doping, interfacial coupling, and so on.[12] Nevertheless, only a handful of studies have been discussed in terms of the in-situ electrochemically self-reconstruction method during the OER process to introduce surficial atoms rearrangement or tetrahedral/octahedral sites occupation transformation for further tuning their ORR electrocatalytic activity. Besides, little attention was paid to the relationship between OER-driven activation and ORR-activity-expression from the perspective of dynamic surface atoms occupation.

Considering all the above reasons, we choose $MnCo_2O_4$ hollow mesoporous nanowires with octahedral/tetrahedral sites and abundant surficial cations deficiencies as an initial model. A series of $MnCo_2O_4$ cubic spinel oxides with various surface tetrahedron and octahedron occupation was then in-situ formed by varying the positive chronoamperometry measurement time (0 h, 1.0 h, 2.0 h, 10 h, and 50 h). These spinel oxides series denoted as $MnCo_2O_4$-pristine ($MnCo_2O_4$-P), $MnCo_2O_4$-1.0, $MnCo_2O_4$-activation ($MnCo_2O_4$-A) $MnCo_2O_4$-10, and $MnCo_2O_4$-50 were used to investigate the relationship between tetrahedral/octahedral occupation and oxygen reduction activity in 0.1 M KOH solution. As expected, tetrahedral/octahedral vacancies on the surface were demonstrated as a key-driven force for surface atoms occupation rearrangement under high electric energy application. Owing to different defects chemical environment, the as-synthesized $MnCo_2O_4$-P with highest Mn/Co octahedron occupation was changed into $MnCo_2O_4$-A, which shows the largest Mn/Co tetrahedron occupation and much more octahedral vacancies because of the refilled tetrahedral deficiencies. Based on related ORR performance analysis, we testify that $MnCo_2O_4$-P and $MnCo_2O_4$-A favored 2 e$^-$ and 4 e$^-$ ORR pathways, respectively. $MnCo_2O_4$-P with the most octahedron occupation presented an excellent ORR performance with high $H_2O_2$ selectivity. It's worth noting that $MnCo_2O_4$-P also gives spectacular durability for ORR test in alkaline electrolyte with an almost invisible LSV shift after 50 h chronoamperometric reaction. Meanwhile, $MnCo_2O_4$-A with most tetrahedron occupation shows a high onset potential of 0.92 V, a high half-wave potential of 0.78 V, a large diffusion-limiting disk current density of 5.0 mA cm$^{-2}$, and excellent stability with negligible activity during ORR measurement as long as 50 h. Significantly, among $MnCo_2O_4$-1.0, $MnCo_2O_4$-A, $MnCo_2O_4$-10, and $MnCo_2O_4$-50, which all go through four electrons transition involved reactions, $MnCo_2O_4$-A was demonstrated as the best-performing one with outstanding ORR activity comparable to that of commercial Pt/C. Density functional theory (DFT) calculations further unraveled that the surface reconstruction from $MnCo_2O_4$-P to $MnCo_2O_4$-A leads to improved

electroactivity due to the increased concentration of tetrahedral Co sites. The modulated electronic structures result in the varied preference in the ORR selectivity in the $2e^-$ and $4e^-$ reduction pathways.

## 2. Results and Discussion

### 2.1. Structure and Morphology Characterizations

$MnCo_2O_4$ spinel oxide with the morphology of hollow mesoporous nanowires was synthesized by a wet-chemical method,[6,13] and the crystal structure was examined by the powder X-ray diffraction (XRD) techniques. As displayed in Figure S1 (Supporting Information), the diffraction peaks fit well with that of the standard $MnCo_2O_4$ (JCPDS card No. 23-1237), suggesting the as-synthesized cobalt manganese oxide possesses a pure cubic spinel phase. The crystal structures show that the unit cell structure consists of both four-oxygen coordinated tetrahedral and six-oxygen coordinated octahedral interstices (Figure S2). The presence of $MnO_4$, $MnO_6$, $CoO_4$, and $CoO_6$ demonstrate $MnCo_2O_4$ a partially inverse spinel structure.[14] In spinel structure ($AB_2O_4$), both the tetrahedral and octahedral sites can provide multiple sites to accommodate different transition-metal cations, thus resulting in a wide range of valence states with the formation of different spinel oxides.[6,15] Furthermore, scanning electron microscopy (SEM) and transmission electron microscopy (TEM) technologies were used to characterize the morphology of the as-prepared $MnCo_2O_4$ nanomaterials. Figure 1a shows the SEM image of $MnCo_2O_4$ nanomaterials, illustrating the assembled flower nanowire structure. As shown in the inset of Figure 1a, $MnCo_2O_4$ nanowires display a hollow structure with rough surfaces. The outer diameter of the nanotube and the thickness of the wall is around 250 nm and 50 nm, respectively. What's more, the large interior channels (diameter of ~150 nm) can further enhance the activity between catalyst surface and oxygen products (Figure S3). In addition, the TEM results (Figure 1b) reveal that $MnCo_2O_4$ nanowires are composed of abundant nanoparticles with the formation of a large amount of mesoporous. Importantly, the average size of these nanoparticles is about 10 nm. The selected area electron diffraction (SAED) pattern (inset of Figure 1b) further reveals the polycrystalline features of $MnCo_2O_4$ hollow mesoporous nanowires with plentiful nanoparticles. A clear lattice fringe with the spacing of 0.475 nm corresponding to the (111) facet of $MnCo_2O_4$ is illustrated by the high-resolution TEM (HRTEM) and the corresponding fast Fourier transforms (FFT), where the observed crystal plane coincides well with XRD patterns (Figure S4). TEM elemental mapping images (Figure 1c) demonstrate that Mn, Co, and O are uniformly and evenly distributed along the hollow mesoporous nanowires.

To further explore the fine structure and the atomic-scale cation distributions of individual $MnCo_2O_4$ hollow mesoporous nanowires, atomic resolution probe aberration-corrected high-angle annular dark-field scanning TEM (HAADF-STEM) images along [1-10], [103], and [121] were directly taken to provide the atom arrangement images (Figure S5-S7). Theoretically, according to the atomic-number differences, atom columns occupied by atoms with a larger atomic number appear brighter in the Z-contrast image when their column thicknesses are the same or similar.[16] Because of the nearly same Z-contrast of Mn atom (Z = 25) and Co atom (Z = 27), it is difficult to directly visualize these two columns from STEM images.[17] Thus, the different brightness between Mn/Co tetrahedral columns and Mn/Co octahedral columns can be attributed to the length of columns, which is the number of atoms for each column. The periodic brightness contrast of all atomic columns in the image of Figure 1d projected from [1-10] orientation is closely correlated with the ordering of cations and spatial distribution in this partially inverse spinel structure. The schematic oriented crystal unit-cell model in the inset of Figure 1d demonstrates not only tetrahedral sites but also octahedral sites are randomly occupied by both Mn and Co (Figure S2). Besides, the corresponding FFT shown in the inset of Figure 1d further confirmed a well-defined partially inverse spinel of $MnCo_2O_4$ oxide. Figure S8 shows clear line intensity profiles marked by the white line, where $Mn^1/Co^1$ represents mixed Mn-Co columns at tetrahedral sites and $Mn^2/Co^2$ represents mixed Mn-Co columns at octahedral sites, respectively. The theoretical simulated STEM images further confirm that the brightness of Mn-Co columns at the tetrahedral sites is brighter than that of Mn-Co columns at the octahedral sites (Figure 1e). Atomic-resolution EDS elemental mappings of $MnCo_2O_4$ in Figure 1f illustrate that metal elements Mn and Co are located at the same geometric sites in the crystal structure of partially inverse $MnCo_2O_4$ spinel oxide (Figure S9). Figure 1g shows the atoms signal intensity distribution image obtained from HAADF-STEM, which is selected from the region with the same atomic layer thickness to eliminate the possible effect of atomic column length and background signal for vacancies determination.[18] The corresponding line scans along with octahedral atomic columns (profile 1 and profile 3) and tetrahedral atomic column (profile 2) directions reveal that both the octahedral and tetrahedral metal defects are presented in the original $MnCo_2O_4$ structure (Figure 1h and Figure S10). While the octahedral metal vacancies seem more obvious than tetrahedral defects. This is because the octahedrally coordinated metals are much more than tetrahedrally coordinated metals (66.7% for octahedron metals and 33.3% for tetrahedron metals)

in a unit cell of $MnCo_2O_4$ (Figure S2). Besides, based on inductively coupled plasma optical emission spectrometry (ICP-OES) analyses, the mainly inherent metal vacancies are proven as Co defects, where Mn:Co molar ratio (1:1.55) obviously deviates from the normal value of 1:2 (Table S1). This special surface vacancies-rich property made partially inverse Mn-Co spinel oxide as an ideal model material for searching excellent catalysts to catalyze oxygen-involved reactions.[19]
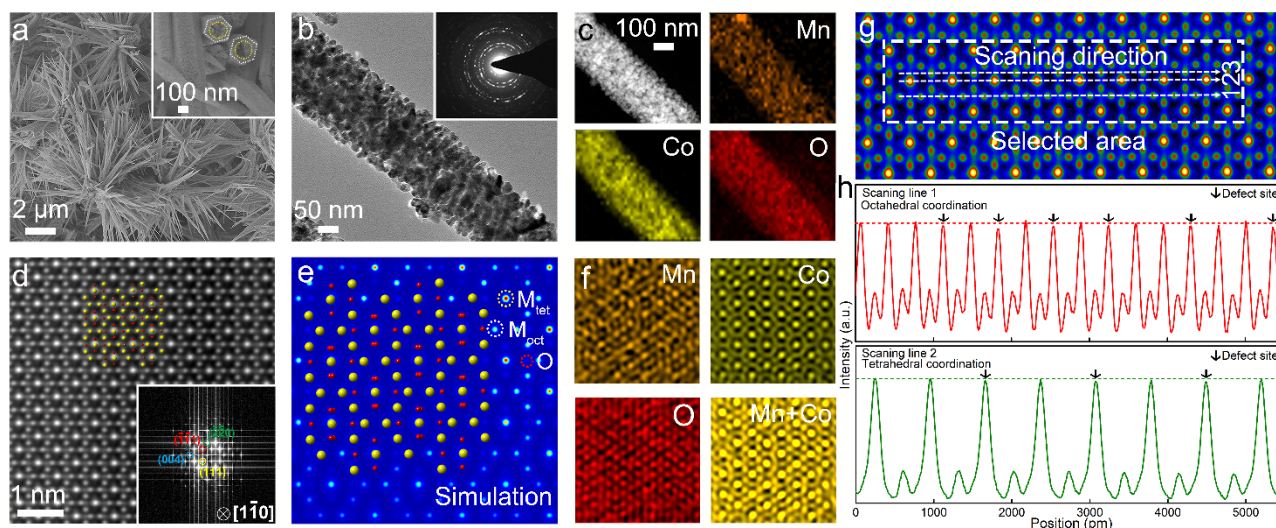


**Figure 1.** (a) SEM, (b) TEM, and (c) EDS elemental mapping images of $MnCo_2O_4$ hollow mesoporous nanowires. Inset of (a) and (b) show the related SEM sectional view and SAED pattern of $MnCo_2O_4$ mesoporous nanowires. (d) Atomic-resolution HAADF-STEM image of the partially inverse spinel $MnCo_2O_4$ structure observed along [1-10] orientation. Inset provides the corresponding FFT pattern and perspective view of the unit cell along [1-10] zone axes. Yellow spheres mean Mn/Co cations at tetrahedral sites or octahedral sites, red spheres represent oxygen atoms. (e) The theoretical STEM images simulated by Quantitative TEM/STEM Simulations Package (QSTEM) software projected along [1-10] orientation. (f) EDS atomic elemental mappings of the as-synthesized $MnCo_2O_4$. (g) The atoms signal intensity distribution from the HAADF-STEM image. (h) The corresponding line scan of numbered profiles 2 and 3 in Figure 1g, respectively.

## 2.2. Electronic Structure Analysis

With the above-mentioned $MnCo_2O_4$ hollow mesoporous nanowires ($MnCo_2O_4$-P) as original model, $MnCo_2O_4$-1.0, $MnCo_2O_4$-2.0, $MnCo_2O_4$-10 and $MnCo_2O_4$-50 samples were in-situ formed via chronoamperometry response by varying measurement time (1.0 h, 2.0 h, 10 h, and 50 h). As shown in Figure 2a, the partial inverse spinel structure is well-maintained during the reaction process, which

is in accordance with the standard $MnCo_2O_4$ (JCPDS card No. 23-1237) confirmed by XRD technology recorded from time-dependent products. However, the peaks' intensity gradually weakens and shows a positive-shift phenomenon with the chronoamperometric testing process going on, which is most visible in the (311) peaks (Figure S11). Besides, the specific surface areas determined by Brunauer-Emmett-Teller (BET) measurement of these $MnCo_2O_4$ spinel oxides series are also found to be related to the chronoamperometric operation time (Table S2). These results are mainly attributed to the reduction in lattice intensity and oxygen atom insertion driven by the OER process, which can provide oxidation activation-dependent surficial structural changes in the properties of $MnCo_2O_4$ spinel oxides, thus influencing the whole adsorption capacity of oxygen-containing intermediates.[20] To verify the cation valence states of Mn/Co in $MnCo_2O_4$ spinel oxides, X-ray absorption near-edge structure (XANES) spectra were performed.[21] As shown in Figure 2b,c, defined by the half-height method,[22] the valence states of Mn and Co in $MnCo_2O_4$-P are situated +3.35 and +2.63, respectively. Herein, according to the charge-balancing mechanism (electric neutrality) in $MnCo_2O_4$, the whole metal valence is +8.61 (much larger than +8), demonstrating the presence of cation vacancies or oxygen excess in the crystal structure. We thus define the real chemical formula for this as-synthesized Co/Mn-occupied spinel oxide approximated as $[Mn_{1-\lambda}^{2+}Co_{\lambda}^{3+}]^T[Mn_{\lambda}^{2+}Co_{2-\lambda}^{3+}]^O O_{4+\delta}$ ($0 < \lambda < 1$; $\delta$ means oxygen non-stoichiometry ranging from 0.20 to 0.35), which is consistent with the results of HAADF-STEM and ICP. As shown in Figure 2d, both the valence states of Mn and Co exhibit a volcano trend with chronoamperometry time going on. The valence of Mn exhibits a mixed state of $Mn^{4+}$ and $Mn^{3+}$; meanwhile, a mixture valence of $Co^{3+}$ and $Co^{2+}$ of Co for these $MnCo_2O_4$ oxides series. Interestingly, the Mn valence decrease in the sequence of $MnCo_2O_4$-P (Mn valence = 3.35) $>$ $MnCo_2O_4$-1.0 (Mn valence = 3.30) $>$ $MnCo_2O_4$-A (Mn valence = 3.24), and then increase gradually from $MnCo_2O_4$-A (Mn valence = 3.24) to $MnCo_2O_4$-50 (Mn valence = 3.32). On the contrary, the valence states of Co show an opposite trend in comparison to Mn (Figure S12 and Table S3). Thus, the shape of the volcano trend can be attributed to the surface arrangement with a 2.0 h-chronoamperometry test giving the most optimal atomic rearrangement on the surface. It's well known that wavelet transform (WT) of EXAFS can discriminate the backscattering atoms and provide high resolution including both radial distances and K-spaces.[23] Two similar intensity maxima at 6.5 $Å^{-1}$ for Mn K edge, meanwhile 6.6 $Å^{-1}$ and 7.0 $Å^{-1}$

for Mn K edge are observed, indicating the same bulk spinel structure for these MnCo-spinel oxides (Figure 2e,f, and Figure S13).

Based on previous findings of CoMn-spinel oxides, Mn/Co valence state is a vital factor for the antibonding orbital occupancy of Mn/Co-O bond, thus the critical role of Mn/Co oxide states can be illustrated by how their electronic structure interacts with the adsorbed-oxygen.[24] Earlier studies have proved that multi-valency of transition metals can be present in not only the octahedral but also the tetrahedral sites.[25] Transition metals cations on the octahedral site can split into low-lying $t_{2g}$ and high-lying $e_g$ orbitals, while the electros in $e_g$ orbital can directly point to O, resulting in a strong spatial overlap with the O 2p orbital. In contrast, in tetrahedral coordination, the spatial overlap of transition metals d-orbital and O 2p orbital is poor, due to the overfilled e antibonding orbitals.[16,19,25] When occupied by two different cations, both the contribution from octahedral sites and tetrahedral sites should not be neglected. Herein, the local structures of Mn/Co in the $MnCo_2O_4$ spinel oxides series were researched by Fourier transform (FT) extended X-ray absorption fine structure (EXAFS) measurement. A perfect match was found for all these electrochemically driven spinel $MnCo_2O_4$ spinel oxides, where Mn/Co-O bond (either at the tetrahedral or octahedral site) is located at $\approx 1.5$ Å; the characteristic octahedra and tetrahedra peaks are around the radial distances of 2.5 Å and 3 Å, respectively (Figure 2g,h, and Figure S14).[26] Based on the fitting results, it's interesting that $\approx 70\%$ Mn and 25% Co cations locate at tetrahedrons and $\approx 30\%$ Mn and 75% Co cations take up octahedrons (Figure 2i and Figure S15). Note for the $MnCo_2O_4$-P, $MnCo_2O_4$-1.0, $MnCo_2O_4$-A, $MnCo_2O_4$-10, and $MnCo_2O_4$-50, both the Mn tetrahedral/octahedral sites occupation and Co tetrahedral/octahedral sites occupation display a volcano trend concerning to chronoamperometry activation time going on. Among these MnCo-spinel oxides, the as-obtained $MnCo_2O_4$-P possess the highest Mn octahedron and Co octahedron occupation, while $MnCo_2O_4$-A has the largest Mn tetrahedron and Co tetrahedron occupation at the same time (Table S4, S5). This further suggests the special surficial atom distribution state of $MnCo_2O_4$-P and $MnCo_2O_4$-A, which may display different activities for oxygen-involved reactions.
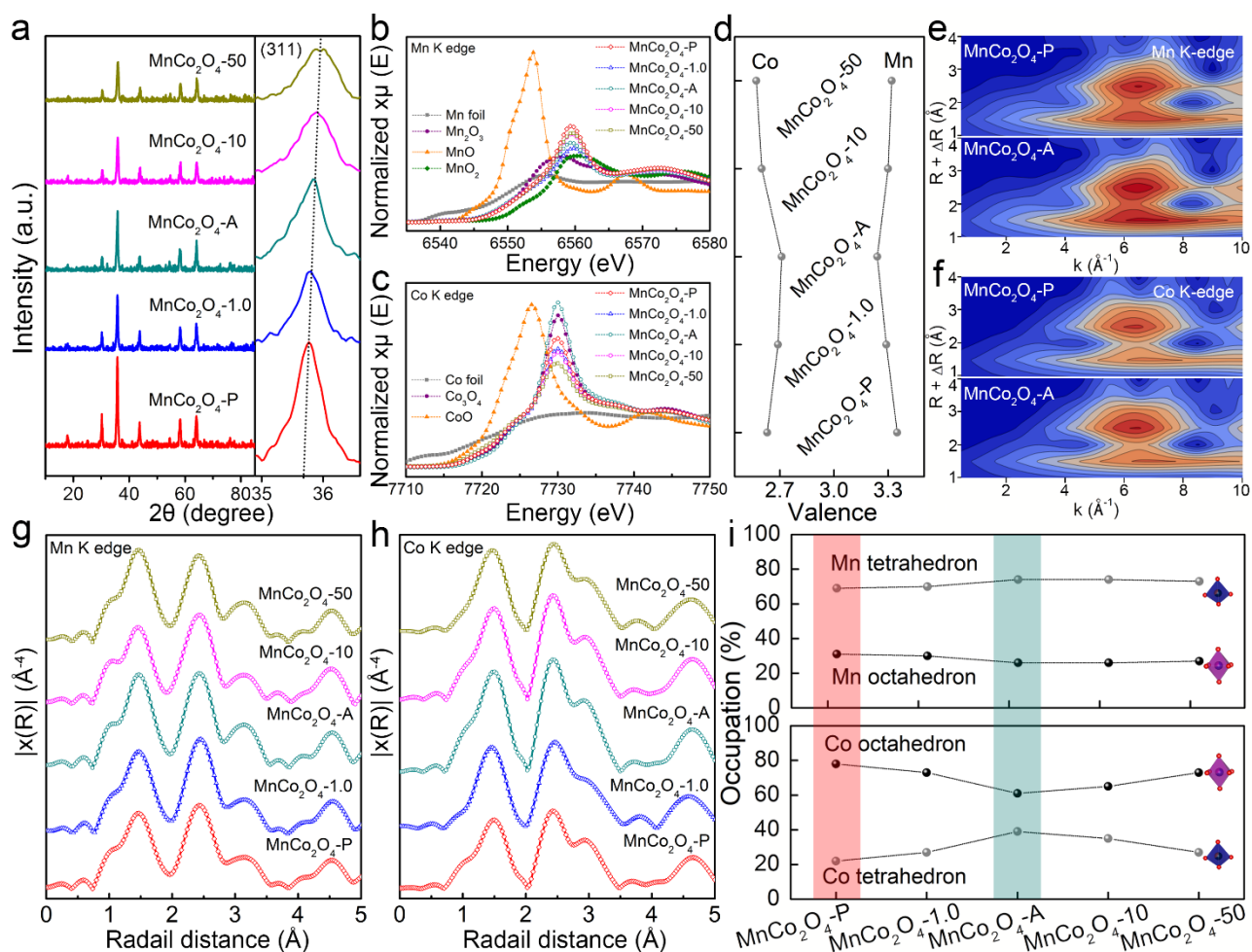
**Figure 2.** (a) XRD patterns of MnCo2O4-P, MnCo2O4-1.0, MnCo2O4-2.0, MnCo2O4-10 and MnCo2O4-50 spinel oxides. The Mn (b) and Co (c) K-edge XANES spectra of these MnCo2O4 oxides series and standard samples. (d) Mn and Co valence state of MnCo2O4-P, MnCo2O4-1.0, MnCo2O4-2.0, MnCo2O4-10, and MnCo2O4-50. Wavelet transforms for the $k^3$-weighted (e) Mn K-edge and (f) Co K-edge EXAFS signals of MnCo2O4-P and MnCo2O4-A. EXAFS $k^3\chi(R)$ spectra of MnCo2O4 oxides series at Mn (g) and Co (h) K-edge. (i) Mn/ Co occupation at tetrahedral and octahedral sites in these MnCo2O4 oxides series, determined by EXAFS fitting.

## 2.3. Surface Structure Analysis

Furthermore, the schematic diagram was made to visualize the morphology evolution process from MnCo2O4-P (nanowires) to MnCo2O4-A (nanotubes), which may provide much more active sites to absorb oxygen-based intermediates and promote electrons transfer (Figure 3a and Figure S16a). Specifically, to track the changes in surface atomic occupations and electronic structures of MnCo2O4 before and after OER activation (2.0 h), we further employed HAADF-STEM technology

and Fast Fourier transform-filtered (FFT-filtered) atomic resolution image for analyzing the surface states of $MnCo_2O_4$-A (Figure 3b and Figure S16b). Figure 3c,d exhibit magnified HAADF-STEM images of $MnCo_2O_4$-A along [1-10] projection acquired from the areas of inside and outside, respectively. It has been found that the interior solid structure of $MnCo_2O_4$ remains unchanged, while the Mn and Co atoms arrangements at the outermost surface exhibit obvious differences (in the left of Figure 3c,d). By analyzing the corresponding FFT patterns of the bulk band and surface region, we prove again the re-constructed interface structure owing to the dynamic evolution of surface atoms (in the middle of Figure 3c,d). X-ray photoelectron spectroscopy (XPS) in Figure 3e reveals a reduction of $Mn^{4+}/Mn^{3+}$ ratio and an increasement of $Co^{3+}/Co^{2+}$ ratio for $MnCo_2O_4$-P and $MnCo_2O_4$-A (Figure S17 and Table S6). Three characteristic Raman peaks at 479 $cm^{-1}$, 516 $cm^{-1}$, and 686 $cm^{-1}$ representing $E_g$, $F_{2g}$, $A_{1g}$ photo models demonstrated the inverse spinel structure of $MnCo_2O_4$ (Figure 3f).[27] However, their Raman spectrum shows no change before and after the OER activation process. This observation can be interpreted by the modified topmost surface and constant main structure of $MnCo_2O_4$, which coincides well with the STEM results. In addition, with $MnCo_2O_4$-A as the study model, a series of electron energy loss spectroscopy (EELS) on both Mn and Co columns are obtained across the boundary in the direction of surface → bulk along [1-10] projection to detail the surface transition process (Figure 3g and Figure S18, S19). These EELS scanning profiles correspond to the selected areas labeled in the range of "1" to "6" in Figure 3b, describing two subregions of spinel oxides at the surface and bulk, respectively. As known, Mn $L_3$-edges and Co $L_3$-edges peaks are associated with the chemical state of Mn and Co ions. Clear chemical shifts of Mn $L_3$-edge and Co $L_3$-edge illustrate the different local chemical environments of these two regions. Furthermore, *in-situ* differential electrochemical mass spectroscopy (DEMS) measurement using isotope $^{18}O$ was used to demonstrate the reaction pathway of $MnCo_2O_4$-P and $MnCo_2O_4$-A, which is dependent on the exposed surficial structure.[28] Their surface was labeled by $^{18}O$ and measured in $^{16}O$ labeled KOH electrolyte. As expected, the ratio of $^{34}O_2$ generated on $MnCo_2O_4$-A ($^{34}O_2/^{32}O_2$ = 3.2%) is greatly different from that of $MnCo_2O_4$-P ($^{34}O_2/^{32}O_2$ = 13.5%), illustrating their different surface structure (Figure S20). In short, the migration scheme of Mn/Co octahedron occupation into Mn/Co tetrahedron occupation of $MnCo_2O_4$-P during the OER process was extracted and visualized in Figure 3h and Figure S21. Triggered by high electric energy, tetrahedral defects can be filled by the nearby octahedron coordinated Mn/Co metals and thus generate much more octahedral vacancies.

Therefore, combined with the EXAFS analysis, we can conclude that as-synthesized $MnCo_2O_4$-P with the highest Mn/Co octahedron occupation possess both tetrahedral and octahedral deficiencies at the same time; while the concentration of tetrahedral and octahedral vacancies in the structure of $MnCo_2O_4$-A with the largest Mn/Co tetrahedron occupation trend to decrease and increase, respectively.
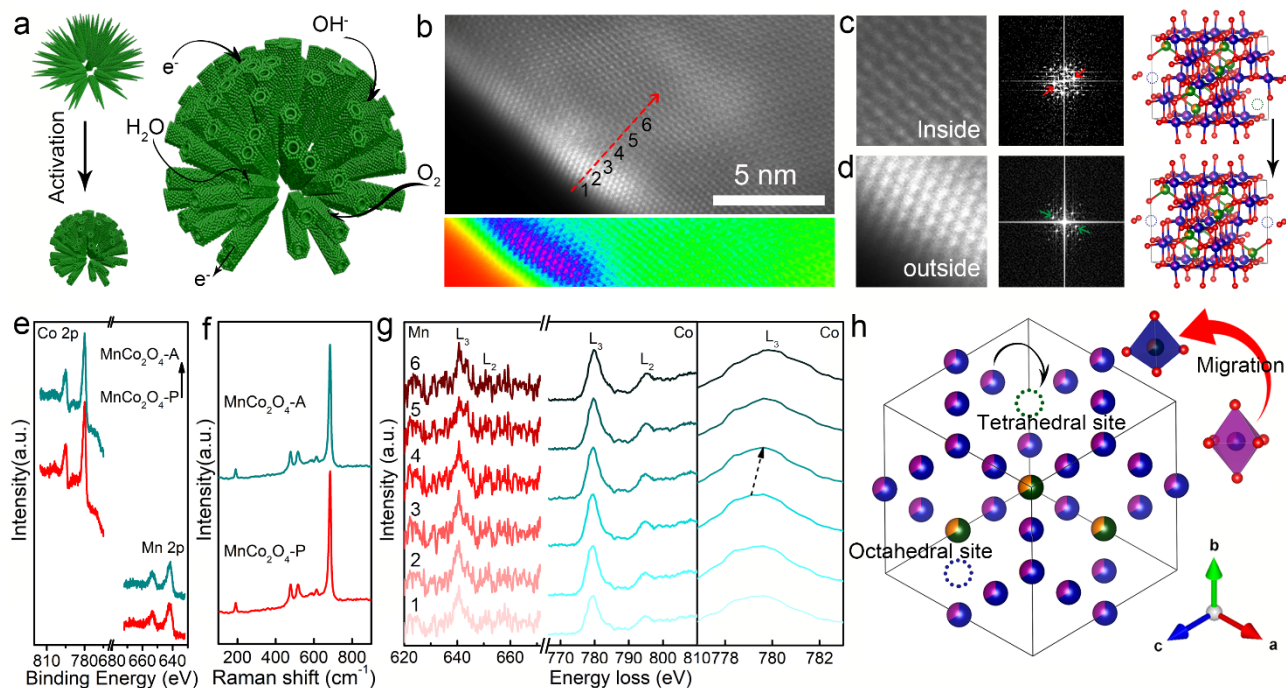


**Figure 3.** (a) Scheme of surface in-situ changes from $MnCo_2O_4$-P to $MnCo_2O_4$-A. (b) HAADF-STEM image close to $MnCo_2O_4$-A surface for the scanning pathway (upper). Scale bar: 5 nm. Fast Fourier transform-filtered (FFT-filtered) atomic resolution image of $MnCo_2O_4$-A (down). (c,d) Magnified HAADF-STEM images of (c) the inside section and (d) the outside section exhibited in (b). The corresponding selected areas' FFTs images. Crystal structure ball & stick model depicting $Mn_1$/$Co_1$ at tetrahedral sites by orange/olive spheres, $Mn_2$/$Co_2$ at octahedral sites by purple/navy spheres, O anions in red spheres, tetrahedral vacancies indicated by green circles, and octahedral vacancies indicated by blue circles, respectively. (e) The Mn 2p XPS spectra and Co 2p XPS spectra of $MnCo_2O_4$-P and $MnCo_2O_4$-A. (f) Raman spectra of $MnCo_2O_4$-P and $MnCo_2O_4$-A. (g) Representative Mn L-edge and Co L-edge EELS spectra along the scanning pathway shown in (b). Selected EELS spectra areas are labeled from 1 to 6 on the STEM image in (b). (h) Occupation rearrangement process from octahedral metals rich surface into tetrahedral metals rich surface.

## 2.4. Electrochemical ORR Performance

The minor surface atoms rearrangement of $MnCo_2O_4$-P was further evaluated by the OER kinetic current density due to that all the catalytic reactions proceed on the surface atoms.[29] The activity $MnCo_2O_4$ series catalysts are assessed in 1.0 M KOH by using alternating voltammetry and chronoamperometry. With the 50-hour stability measurement by chronoamperometry holds at 1.60 V *vs*. RHE, Figure S22a shows sample cyclic voltammograms (CVs) taken periodically during testing at different times. Figure S22b exhibits a Tafel plot of the intrinsic specific activities for all these materials throughout the stability test, and further compared with the best reported and commonly used catalysts ($IrO_2$) in alkaline electrolytes. The Tafel slope of $MnCo_2O_4$-A (45.27 mV dec$^{-1}$), which is much smaller than that of $MnCo_2O_4$-P (88.31 mV dec$^{-1}$), $MnCo_2O_4$-1.0 (85.79 mV dec$^{-1}$), $MnCo_2O_4$-10 (53.15 mV dec$^{-1}$), and $MnCo_2O_4$-50 (55.07 mV dec$^{-1}$), revealing that there was obvious surface rearrangement during the activated process. However, it is reasonable that there presents an optimal activation state ($MnCo_2O_4$-2.0-hour chronoamperometric measurement) and excessive activation goes against the catalytic property enhancement as required potentials mapped in Figure S22c. This volcano tendency gives the relationship between $MnCo_2O_4$ oxides series and their activity with $MnCo_2O_4$-A showing the best performance. Some amorphous layers attributed to metal oxyhydroxides can be found in HAADF-STEM images of $MnCo_2O_4$-50 (Figure S23). We thus believe that surficial atoms migration between octahedral and tetrahedral sites is a critical transition step for generating amorphous structure and the excessive reconstruction is disadvantageous to activity promotion. This is also in line with the EXAFS results of $MnCo_2O_4$-10 and $MnCo_2O_4$-50 showing gradually enhanced Mn/Co octahedron occupation since in-situ formed metal oxyhydroxides are composed with edge-sharing $MO_6$ octahedral structure.[26,30] Additionally, if ignoring other possible capacitance contributions such as pseudo-capacitance (caused by ion adsorption and intercalation) or chemical capacitance (caused by a population of electron trap states), the electrochemically active surface area (ECSA) of each catalyst can be evaluated by double-layer capacitance ($C_{DL}$) measurement within about an order of magnitude.[31] With the same crystal structure, we thus attribute the change on the ECSA of $MnCo_2O_4$ series into their changeable surface atoms arrangement states (Figure S24 and Table S7).

The electrocatalytic performances of $MnCo_2O_4$-P and series OER process modified $MnCo_2O_4$ for oxygen reduction are evaluated in $O_2$-saturated 0.1 M KOH electrolyte using a rotating disk

electrode (RDE).[32] To estimate their catalytic activities, the corresponding linear sweep voltammograms (LSVs) are extracted by averaging the positive-going and negative-going CVs.[33] Then, typical ORR polarization curves of these $MnCo_2O_4$ after background- and iR-correction are shown in Figure 4a. It should be mentioned that the conductive carbon (e.g., acetylene black) shows an insignificant contribution to such current with rather a negligible background current from carbon (Figure 4a and Figure S25). As expected, the ORR performance of $MnCo_2O_4$-A with an onset potential of 0.92 V, a half-wave potential of 0.78 V, and a diffusion-limiting disk current density of 5.0 mA $cm^{-2}$ is much superior to commercial Ir/C (20%) catalyst and comparable to Pt/C (20%) catalyst. In detail, $MnCo_2O_4$-P needs a potential of 0.66 V to reach 3 mA $cm_{disk}^{-2}$ and positively enhance to 0.69 V after 1.0-hour OER testing. The catalyst continues to increase in activity within the 2.0-hour OER chronoamperometric measurement and requires a much positive reduction potential of 0.76 V to this current density. On the contrary, activity deteriorations are detected with stability measurement going on, as indicated by the negative-shift potential (of 0.73 V for $MnCo_2O_4$-10 and 0.71 V for $MnCo_2O_4$-50) to meet 3 mA $cm_{disk}^{-2}$ for the remainder of the measurements, illustrating the superior ORR catalytic activity of $MnCo_2O_4$-A with surface atom modification (Figure S26). It is well known that mass activity (MA) and the turnover frequencies (TOF) can be used as reliable descriptors to evaluate performances toward various catalysts.[34] Herein, MA and TOF are mapped out in Figure 4b with $MnCo_2O_4$-A exhibiting the highest values. Based on the Koutechy−Levich (K−L) equation, rotating-speed-dependent ORR polarization curves of $MnCo_2O_4$ series oxides were made to calculate the electron transferred number (n) and kinetic current density ($j_k$) (Figure 4c,d, and Figure S27). Of notable interest is that $MnCo_2O_4$-A shows the highest $j_k$ (92.94 mA $cm^{-2}$ at 0.45 V and 83.40 mA $cm^{-2}$ at 0.40 V), which is much larger than those of $MnCo_2O_4$ series oxides; besides, the slopes of Koutechy−Levich (K−L) plots indicate the two electrons ORR reaction and direct four electrons transfer pathway for $MnCo_2O_4$-P and $MnCo_2O_4$-A, respectively. A rotating ring disk electrode (RRDE) was further used to detect the n and $H_2O_2$ yield for the ORR process of $MnCo_2O_4$-P and $MnCo_2O_4$-A in 0.1 M $O_2$-saturated KOH (Figure S28). As observed, the calculated electron numbers for $MnCo_2O_4$-P and $MnCo_2O_4$-A are 2.43 (close to 2) and 3.96 (approach to 4), further confirming their favored 2 $e^-$ ORR and 4 $e^-$ ORR pathway, respectively (Figure S29).[21] In addition, for $MnCo_2O_4$-P, the $H_2O_2$ selectivity ($H_2O_2$%) remains at $\approx$ 80% in a wide potential range and reaches nearly 100 % at 0.75 V vs. RHE (Figure S30). These results confirm an ideal 2$e^-$ reaction

pathway for the as-synthesized $MnCo_2O_4$ to produce fundamental chemicals $H_2O_2$, which is an important chemical.[2,5,35]

Importantly, both $MnCo_2O_4$-P with 2 e$^-$ ORR pathway and $MnCo_2O_4$-A with 4 e$^-$ ORR pathway shows excellent stability for 50 h in 0.1 M KOH at 0.4 V without obvious potential change (Figure S31). After this long-term stability test, a negligible LSV shift is observed for both $MnCo_2O_4$-P and $MnCo_2O_4$-A (Figure 4e,f, and Figure S32), and their composition, morphology, and electronic structure show unnoticeable change as depicted in Figure S33, indicating the stable structure of CoMn-spinel oxides against the oxidation-reduction process. As exhibited in Figure 4g,h, the main peaks of $MnCo_2O_4$ were almost unchanged during in-situ Raman tests under decreased voltages in sequence from 0.95 V to 0.15 V in $O_2$-saturated alkaline media (Figure S34), further illustrating that the main crystal structure of Co-Mn spinel oxides can keep stable under different potentials. Furthermore, compared with $MnCo_2O_4$-P (Figure 1c), the EDS elemental mappings suggested an increased Mn and Co contents on the surface of $MnCo_2O_4$-A and $MnCo_2O_4$-A after ORR stability measurement, which indicates the self-optimized surficial atoms occupation during the activation process and this re-modified surface is stable during ORR in the basic electrolyte (Figure S35, S36). Of note, both the $MnCo_2O_4$-P and $MnCo_2O_4$-A stand out from or are comparable to the most recently reported 2e$^-$ ORR and 4 e$^-$ ORR electrocatalysts, respectively (Table S8, S9). All these results indicate $MnCo_2O_4$-P and $MnCo_2O_4$-A as superb 2 e$^-$ and 4 e$^-$ oxygen reduction electrocatalysts, respectively; meanwhile, the ORR pathway of spinel oxides via two electrons transfer or four electrons transfer can be selected by surface atom modification (Figure 4i). We thus believe that although the same composition and crystal structure, all these $MnCo_2O_4$ spinel oxides display different intrinsic electrochemical activities, which proves that the effect of Mn/Co cations on octahedral or tetrahedral sites and the Mn/Co valence are formidable on the ORR activity of spinel oxides.
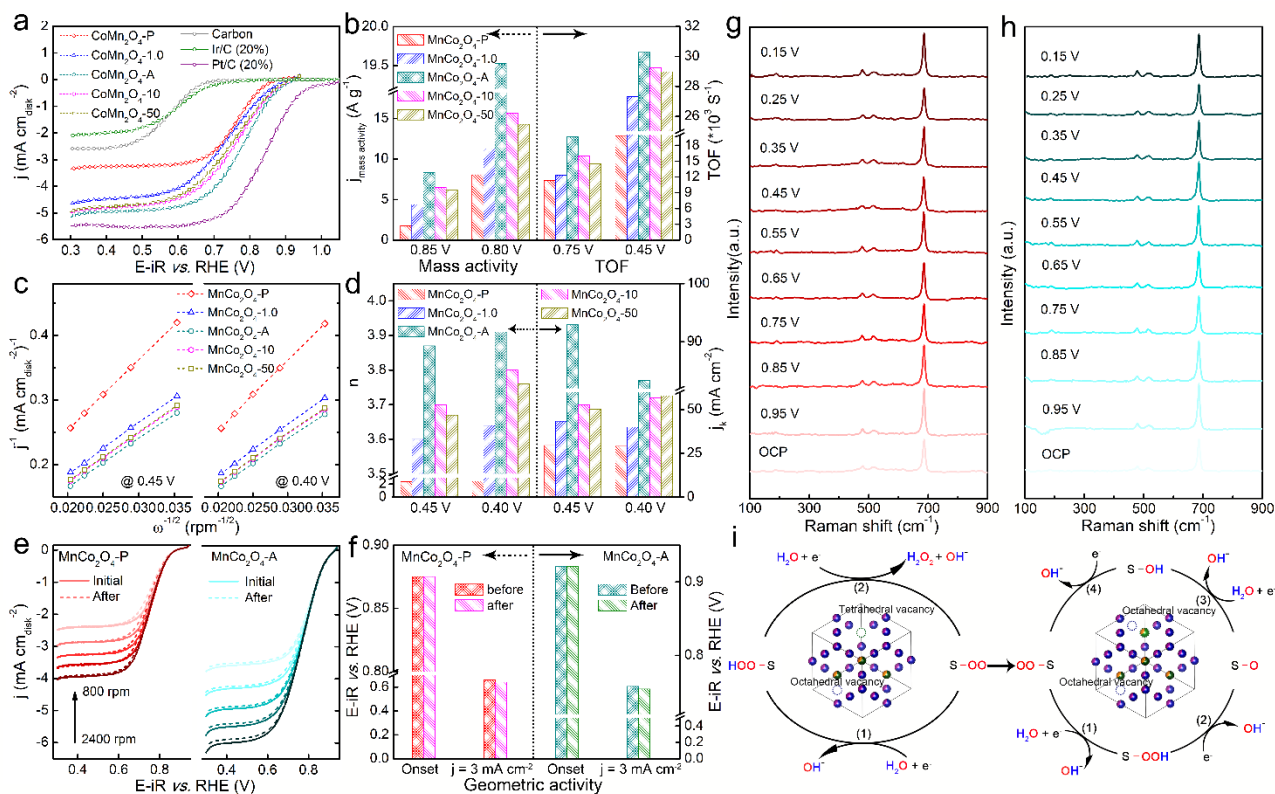
**Figure 4.** (a) LSV curves after background-correction and iR-correction of $MnCo_2O_4$-P, $MnCo_2O_4$-1.0, $MnCo_2O_4$-A, $MnCo_2O_4$-10, and $MnCo_2O_4$-50 for ORR performed in 0.1 M KOH (scan rate: 10 mV s$^{-1}$, rotating speed: 1600 rpm). (b) The activity comparisons in mass activity at 0.85 V and 0.80 V (vs. RHE) and TOF at 0.75 V and 0.45 V (vs. RHE) for these $MnCo_2O_4$ series. (c) The K−L plots of these $MnCo_2O_4$ series at 0.45 V and 0.40 V vs. RHE. (d) Calculated n and $j_k$ for these $MnCo_2O_4$ series in ORR. (e) ORR polarization curves of $MnCo_2O_4$-P and $MnCo_2O_4$-A at different rotating speeds (800 rpm, 1200 rpm, 1600 rpm, 2000 rpm, and 2400 rpm) before and after a chronoamperometric measurement for 50 hours. (f) The corresponding parameters were obtained from (e) at the rotation rate of 1600 rpm. In-situ Raman of (g) $MnCo_2O_4$-P and (h) $MnCo_2O_4$-A. (i) Scheme of ORR reaction paths for $MnCo_2O_4$-P and $MnCo_2O_4$-A.

## 2.5. Theory Calculations

In fact, not all electrocatalysts will undergo surface reconstruction under OER conditions, some stable catalysts have also been reported, whose active sites didn't affect by the high oxidation potentials.[36] It is thus urgent to uncover the origin of the surface evolution of Mn-Co spinel oxides. To further confirm why the surficial geometrical occupation of $MnCo_2O_4$ with metal defects rich

surface can be easily tunned to realize the ORR reaction pathway transformation from 2e⁻ to 4 e⁻ processes, electronic density of states (DOS) calculations for pristine $MnCo_2O_4$ was constructed in Figure S37. To be specific, both the tetrahedral and octahedral vacancies ensure cation deficient $MnCo_2O_4$ showing excellent conductivity. Not only metal d electrons, but also O p electrons are observed across the Fermi level. By integrating, the O p electrons for spin up (55.12) cannot offset the electrons for a spin down (-53.38), revealing the presence of an O hole favoring further surface atoms reconstruction.[37] We thus believe the abundant cation defects would be the driving force for surface metal occupation rearrangement.

To investigate the ORR performances of the $MnCo_2O_4$, we have carried out DFT calculations regarding the electronic structures and reaction trends in $MnCo_2O_4$-P and $MnCo_2O_4$-A. For $MnCo_2O_4$-P, the surface electronic distributions near the Fermi level ($E_F$) have been demonstrated, where the surface abundant vacancies can induce strong perturbations to the electronic structures of $MnCo_2O_4$-P (Figure 5a). In contrast, $MnCo_2O_4$-A displays a more electron-rich surface due to the surface reconstructions than $MnCo_2O_4$-P, leading to a stronger reduction capability (Figure 5b). The different surface electronic structures induced by the reconstructions of tetrahedral and octahedral sites result in the distinct selectivity of ORR. Then, we further compare the detailed electronic contributions of different elements. In $MnCo_2O_4$-P, we notice that Co-3d shows the evident peak at $E_V$-1.10 eV ($E_V = 0$ eV), which plays as the active site for the ORR (Figure 5c). In the meantime, Mn-3d orbitals have shown the $e_g$-$t_{2g}$ splitting of 3.23 eV, which protects the Co-3d peaks for a robust valence state. O-2p orbitals locate at the deepest position as the electron reservoir. After surface reconstruction, we notice that the electronic structure of both Mn and Co has been modulated (Figure 5d). Co-3d orbitals in $MnCo_2O_4$-A become more electroactive with a closer distance to $E_F$ at $E_V$-0.57 eV, supporting the increased valence states in Co with improved reduction capability. However, the $e_g$-$t_{2g}$ splitting of Mn-3d orbitals has been enlarged to 4.10 eV in $MnCo_2O_4$-A. Notably, the overall O-2p orbitals have not been strongly affected. To further understand the influences of the surface reconstruction, we have compared the site-dependent PDOS in $MnCo_2O_4$ regarding both the octahedral and tetrahedral sites (Figure 5e). From the bulk to the surface, Co-3d in the octahedral sites shows a gradual upshifting trend towards the Fermi level, indicating the improved electroactivity. In comparison, the tetrahedral Co sites show a higher electroactivity, which remains stable from bulk to the surface. These results indicate that the tetrahedral Co sites show stronger

contributions to the electroactivity. The higher concentrations of tetrahedral Co sites in $MnCo_2O_4$-A lead to a stronger reduction trend of ORR towards the $4e^-$ pathway. Meanwhile, Mn sites in both tetrahedral and octahedral sites deliver a similar trend (Figure 5f). From the bulk to the surface, the $e_g$-$t_{2g}$ splitting of Mn-3d orbitals gradually increases, which is more evident in the tetrahedral sites. Then, the O-2p orbitals on the surface are also activated by the vacancies and surface modulations (Figure 5g). On the surface, the O sites near the reconstruction metals and vacancies display a higher p-band center than the bulk and near-surface O sites. These results confirm that the surface reconstructions induce evident modulations on the electronic structures of $MnCo_2O_4$, which determines the different reaction pathways of ORR. Furthermore, the PDOS of the key adsorbates also indicates distinct reaction trends (Figure 5h,i). For $MnCo_2O_4$-P, we notice that the linear correlation is formed towards the formation of $H_2O_2$ rather than O*, which demonstrates an improved electron transfer efficiency for the $2e^-$ ORR pathway. For $MnCo_2O_4$-A, we notice that the conversion of the $4e^-$ pathway exhibits an obvious linear correlation while the generation of $H_2O_2$ has deviated from the correlation. This difference in electron transfer efficiency reveals that $MnCo_2O_4$-A and $MnCo_2O_4$-P are prone to $4e^-$ and $2e^-$ ORR pathways, respectively, which are supportive of the experimental characterizations. From the energetic perspective, the $MnCo_2O_4$-P delivers lower formation energy than $MnCo_2O_4$-A, which explains that electrochemical activation of OER is needed for the synthesis of $MnCo_2O_4$-A (Figure 5j). Then, the reaction energies of the $4e^-$ ORR pathway have been compared, in which we notice that $MnCo_2O_4$-A shows a larger onset potential (0.89 V) than $MnCo_2O_4$-P (0.60 V) to drive the ORR reaction, indicating a much-improved electroactivity of $MnCo_2O_4$-A in the $4e^-$ ORR pathway (Figure 5k). In comparison, the selectivity towards $H_2O_2$ has been compared under the equilibrium potential (0.70 V) for both $MnCo_2O_4$-A and $MnCo_2O_4$-P (Figure 5l). Notably, $MnCo_2O_4$-P only shows a subtle energy barrier of 0.09 eV for the generation of $H_2O_2$, supporting the high selectivity. The much higher energy barrier of 0.37 eV in $MnCo_2O_4$-A leads to the stronger selectivity of the $4e^-$ ORR pathway instead of the $2e^-$ ORR pathway. Therefore, DFT calculations have reflected the electronic modulations induced by surface reconstructions and their corresponding influences on the selectivity of the ORR process.
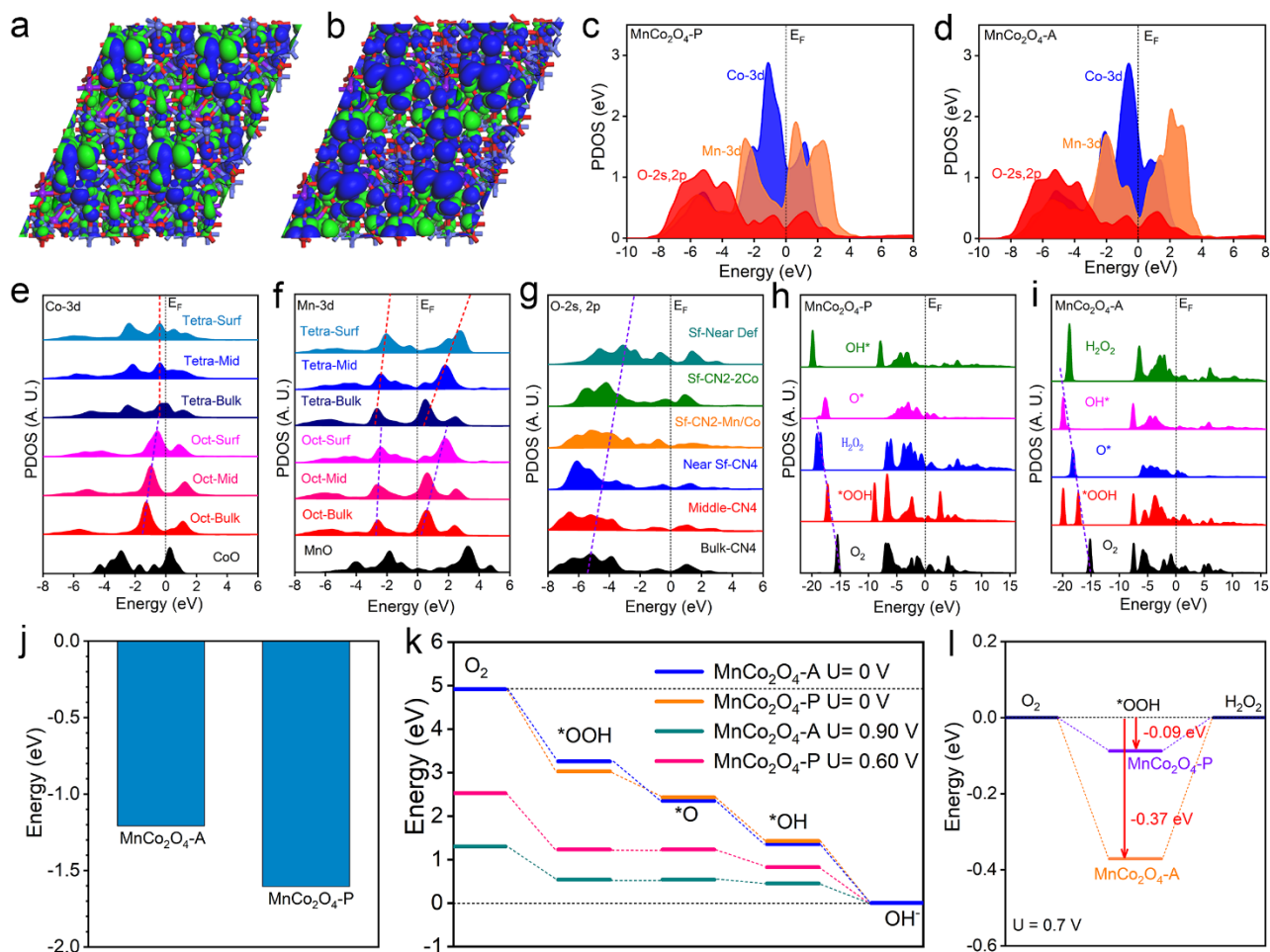
**Figure 5.** The 3D contour plot of electronic distribution near Fermi level of (a) MnCo$_2$O$_4$-P and (b) MnCo$_2$O$_4$-A. Purple balls= Mn, blue balls = Co and red balls = O. Blue isosurface = bonding orbitals and green isosurface = anti-bonding orbitals. The PDOS of (c) MnCo$_2$O$_4$-P and (d) MnCo$_2$O$_4$-A. (e) The site-dependent PDOS of Mn-3d in MnCo$_2$O$_4$-A. (f) The site-dependent PDOS of Co-3d in MnCo$_2$O$_4$-A. (g) The site-dependent PDOS of O-s,p in MnCo$_2$O$_4$-A. (h) The PDOS of key adsorbates in MnCo$_2$O$_4$-A. (i) The site-dependent PDOS of O-s,p in MnCo$_2$O$_4$-P. (j) The formation energies of MnCo$_2$O$_4$-P and MnCo$_2$O$_4$-A. (k) The ORR reaction energy trend for MnCo$_2$O$_4$-P and MnCo$_2$O$_4$-A. (l) The reaction trend for H$_2$O$_2$ generation under U=0.70 V.

## 3. Conclusions

In summary, using partially inverse spinel MnCo$_2$O$_4$ as a pristine model, we synthesized a class of surface tunned Mn-Co spinel oxides (MnCo$_2$O$_4$-1.0, MnCo$_2$O$_4$-A, MnCo$_2$O$_4$-10, and MnCo$_2$O$_4$-50) via in-situ electrochemical modification. Owing to the abundant tetrahedral and octahedral vacancies, the surface of MnCo$_2$O$_4$-P with the highest Mn/Co octahedron occupation was changed into

MnCo$_2$O$_4$-A with the largest Mn/Co tetrahedron occupation. Besides, we show tuning surface metal cations occupation of MnCo$_2$O$_4$ gives the ORR catalytic response from 2 e$^-$ ORR to 4 e$^-$ ORR pathways. In detail, MnCo$_2$O$_4$-P through 2 e$^-$ ORR pathway shows high H$_2$O$_2$ selectivity, and MnCo$_2$O$_4$-A via 4 e$^-$ ORR route possesses a high onset potential of 0.92 V and half-wave potential of 0.78 V, which is comparable to that of commercial Pt/C. In addition, both MnCo$_2$O$_4$-P and MnCo$_2$O$_4$-A via different reaction mechanisms exhibit excellent stability. DFT calculations have demonstrated that the electrochemical activated MnCo$_2$O$_4$-A exhibited improved electron transfer towards the complete reduction of O$_2$ while the MnCo$_2$O$_4$-P shows the lower d-band center with higher selectivity towards the formation of H$_2$O$_2$. Both electronic structures and reaction energies have revealed the distinct selectivity induced by the surface reconstruction in MnCo$_2$O$_4$. This work provides us an attractive perspective to understand the surface effect and offers a vital relationship between OER activation and ORR activity, which thus opens a new avenue to design superior electrocatalysts with special purposes.

## 4. Experimental Section

*Materials:* MnCl$_2$·4H$_2$O (99.0 %), CoCl$_2$·6H$_2$O (98.0 %), CO(NH$_2$)$_2$ and Nafion® (5 wt%) were obtained from Aladdin. The deionized (DI) water was obtained from a Millipore Autopure system (18.2 MΩ, Millipore Ltd., USA). All the other materials for electrochemical measurements were of analytical grade and without further purification.

*Material synthesis:* MnCl$_2$·4H$_2$O (1 mmol), CoCl$_2$·6H$_2$O (2 mmol), and CO(NH$_2$)$_2$ (10 mmol) were dissolved in deionized water (40 ml) to form a homogeneous solution under vigorous magnetic stirring. After stirring for 30 min, the as-obtained solution was transferred into a 60 ml Teflon-lined stainless-steel autoclave, followed by heating the autoclave in an electric oven at 120 °C for 16 h. After being cooled to room temperature, the products were taken out, ultrasonically cleaned for 5 min in the DI water, rinsed with ethanol several times, dried at 80 °C overnight, and then annealed at 400 °C in the air for 3 hours. We start by tuning the surface electronic structure of MnCo$_2$O$_4$ cubic spinel oxides by varying the chronoamperometry measurement time (0 h, 1.0 h, 2.0 h, 10 h, and 50 h) at 1.6 V vs. RHE.

*Characterizations:* Powder X-ray diffraction (XRD) patterns were collected on a Rigaku D/Max-2400 diffractometer with Cu-Kα radiation (λ = 1.54178 Å) from 10º to 90º under a constant voltage

of 40 kV. The scanning electron microscope (SEM) images were obtained by the JEOL JSM 6700F electron microscope with an accelerating voltage of 5 kV. Transmission electron microscopy (TEM) and high-resolution transmission electron microscopy (HRTEM) images were collected on Tecnai G2 F30 Field Emission Transmission Electron Microscope. Atomic-scale STEM images were recorded on a probe aberration-corrected STEM (Cubed Titan G2 60-300, FEI, USA) operated at 300 kV. X-ray photoelectron spectroscopy (XPS) was carried out on a VG ESCALAB 220I-XL device with Mg K$\alpha$ ($hv$ = 1253.6 eV) as the excitation source. The binding energies obtained in the XPS spectral analysis were corrected for specimen charging by referencing C 1s to 284.8 eV. The standard deviation for the binding energy (BE) values was 0.1 eV. $N_2$ adsorption/desorption measurement was determined at 450 $^{\circ}$C using an Autosrob-1 (Quantachrome INSTRUMENTS). Inductively coupled plasma optical emission spectrometry (ICP-OES) analyses were performed on a Plasma Quant PQ9000 ICP spectrometer. The X-ray absorption fine structure spectra (at the Co, Mn K-edge) analyses were performed at 1W1B station in Beijing Synchrotron Radiation Facility (BSRF) using a Si (111) double-crystal monochromator. The storage rings of NSRF were operated at 2.5 GeV with a maximum current of 250 mA.

*X-ray absorption spectroscopy:* Data merging, normalization, and fitting of the XANES and EXAFS spectra were performed using the Demeter software package. The data reduction and data analysis were performed with the Athena, Artemis, and IFEFFIT software packages. The $k^3$-weighted Fourier transforms for all the EXAFS data were conducted in the k-range 2–12 Å$^{-1}$. EXAFS were fitted using the normal spinel $MnCo_2O_4$ structure as the starting structure model. The R-ranges for the fitting of all the EXAFS data were set as 1.0–2.0 Å. The edge position was accurately estimated by an integral method in the range 0.15~1.0 normalized $\chi\mu$ (E), where $\mu$ is the normalized absorbance. In this case, with standard CoO, $Co_3O_4$ (Sigma Aldrich) as a reference, Co valence was calculated by the formula of Co Valence = (Energy-7720.293798) / (7723.508407-7720.293798) * (8/3-2) + 2; and according to the standard $MnO_2$, $Mn_2O_3$ (Sigma Aldrich), we use Mn Valence = (Energy-6551.01206719989)/(6554.06949-6551.01206719989)*(4-3)+3 to obtain the valence of Mn. Atom distribution function (ADF) method,[38] whose spatial resolution is three times higher than the conventional methods, was applied to obtain site occupancy from EXAFS fitting. To be specific, Mn and Co K-edge at the same sample were fitted simultaneously. The site occupancy of Mn and Co was described by one parameter, the number of Mn and Co at tetrahedral sites or octahedral sites. The Mn

occupancy ($x_{Mn}$) and Co occupancy were analyzed based on the method reported by a reported reference.[39]

*Electrode preparation:* The as-synthesized catalysts were firstly loaded on carbon support by sonicating the catalysts/carbon mixture in hexane (the loading amount of catalyst is kept around 50 w/w %) for 3 hours. After collecting the sediment of carbon-supported catalysts, 3 mg catalysts/carbon catalyst was ultrasonically dispersed in 1470 $\mu$L DMF solvent with 30 $\mu$L Nafion as the binder to form a 2 $mg_{catalysts+C} \cdot mL^{-1}$ ink. 12.6 $\mu$L of the catalyst ink (containing 25.2 $\mu$g of catalyst) was drop-casted onto a glassy carbon (GC) electrode with a diameter of 4 mm (the carbon-supported catalyst loading mass is 0.2 $mg \cdot cm^{-2}$) and dried at ambient condition.

*Electrochemical Measurements:* All electrochemical measurements were performed with a three-electrode system using a CHI760 Electrochemical Workstation (CHI Instruments, Shanghai Chenhua Instrument Corp., China). For the electrocatalytic OER in $O_2$-saturated basic media (1.0 M KOH) and ORR (0.1 M KOH), a Pt electrode and Hg/HgO (1.0 M KOH) were used as counter and reference electrodes. The reference electrode is previously calibrated in $H_2$ saturated electrolyte with respect to an in-situ reverse hydrogen electrode (RHE), by using platinum wires as working electrodes, which yields the relation $E_{RHE} = E_{(Hg/HgO)} + 0.098 + 0.0591pH$. All electrochemical experiments were conducted at $20 \pm 0.2$ °C. To analyze ORR performance, the rotating disk electrode (RDE) was used as a working electrode by applying different rotating speeds (800 rpm, 1200 rpm, 1600 rpm, 2000 rpm, and 2400 rpm) within a potential window of 1.0-0.3 V vs. RHE. To investigate the electron transfer number (n) and reaction pathway for ORR, rotating ring-disk electrode (RRDE) voltammograms were conducted on an RRDE configuration (RRDE–3A, Japan) consisting of a glassy carbon disk electrode and a Pt ring electrode. A scan rate of 10 mV $s^{-1}$ and a rotation rate of 1600 rpm was applied for RRDE tests, while the ring potential was held constant at 1.5 V vs. RHE to capture hydrogen peroxide ($H_2O_2$).[40] The working electrodes were scanned several times until the signals were stabilized, then Cyclic voltammogram (CV) data were collected, corrected for the *iR* contribution within the cell. ORR activities of oxides were extracted by averaging the negative-going and positive-going CVs scan (disk) in $O_2$-saturated 0.1M KOH at a rotating speed of 1600 rpm.[41] The surface areas of spinel oxides were determined by the electrochemically active surface area (ECSA). Electrochemical capacitance was determined using cyclic voltammetry (CV) measurements. This range at the non-Faradaic current response region is typically a 0.1 V window centered at the

OCP of the system. The different scan rates were selected as 0.01, 0.05, 0.1, 0.3 and 0.5 V s$^{-1}$. The ECSAs of all these catalysts can be calculated via dividing $C_{dl}$ by the specific capacitance of the sample as shown in the following equation: ECSA = $C_{dl}/C_s$, where we use the general specific capacitance of 60 $\mu F$ cm$^{-2}$, which is considered universal for oxide surfaces.[42,43]

*The RDE measurements:* The mass transport correction and the relationship between the measured currents (j) with various rotating speeds (ω) under fixed potentials was performed employing the well-known Koutechky-Levich (K-L) equation:[40]

$$1/i_{measure} = 1/i_k + 1/i_d$$

or

$$1/j = 1/j_k + 1/B\omega^{1/2}$$

Where $j_k$ is the kinetic current and ω is the electrode rotating rate. B is determined from the slope of the Koutechy-Levich (K-L) plots based on the Levich equation below:

$$B = 0.2nF(D_{O2})^{2/3}v^{-1/6}C_{O2}$$

where n represents the transferred electron number per oxygen molecules. F is the Faraday constant (F = 96485.3 C mol$^{-1}$). $D_{O2}$ is the diffusion coefficient of $O_2$ in 0.1 M KOH ($D_{O2}$ = 1.9 × 10$^{-5}$ cm$^2$ s$^{-1}$). v is the kinetic viscosity (v = 0.01 cm$^2$ s$^{-1}$). $C_{O2}$ is the bulk concentration of $O_2$ ($C_{O2}$ = 1.2 × 10$^{-6}$ mol cm$^{-3}$). The constant 0.2 is adopted when the rotation rate is expressed in rpm.

*The RRDE measurements:* the disk electrode was scanned at a rate of 10 mV s$^{-1}$, and the ring potential was constant at 1.5 V vs. RHE. The %HO$^{2-}$ and transfer number (n) were determined by the followed equations:[40]

$$\%HO_2^- = 200I_r/(I_dN + I_r)$$

$$n = 4NI_d/(NI_d + I_r)$$

where N is the collection efficiency of the rotating ring disk electrode (Pt ring), $I_d$ is disk current, and $I_r$ is ring current. N was determined to be 0.40.

*Calculation of turnover frequency (TOF) and mass activity:* The mass activity (A g$^{-1}$) values were calculated from the catalyst building m (mg cm$^{-2}$) and the measured current density j (mA cm$^{-2}$) at 0.80 V and 0.85 V vs. RHE:[40]

$$\text{mass activity} = j/m$$

The TOF values were calculated by assuming that every metal atom is involved in the catalysis (lower TOF limits were calculated):

$$TOF = jS/4nF$$

where j (mA cm$^{-2}$) is the measured current density at 0.45 V and 0.75 V vs. RHE, S is the surface area of the working electrode, the number 4 means 4 electrons mol$^{-1}$ of O$_2$, F is Faraday's constant (96485.3 C mol$^{-1}$), and n is the moles of coated metal atom on the electrode calculated from m.

*Calculation Setup:* To study the formation and electrochemical performances of MnCo$_2$O$_4$-A and MnCo$_2$O$_4$-P, DFT calculations have been introduced based on the CASTEP packages regarding the modulations on electronic structures and energetic trends[44]. In this work, the generalized gradient approximation (GGA) and Perdew-Burke-Ernzerhof (PBE) have been used to reach accurate descriptions of the exchange-correlation interactions[45-47]. Meanwhile, we have set the plane-wave basis cutoff energy to 380 eV based on the ultrasoft pseudopotentials for all the geometry optimizations. The Broyden-Fletcher-Goldfarb-Shannon (BFGS) algorithm is applied for all the energy minimizations[48] with the coarse quality of k-points to optimize the balance between calculation efficiency and accuracy. Both MnCo$_2$O$_4$-P and MnCo$_2$O$_4$-A models have been constructed based on the (111) surface of the MnCo$_2$O$_4$ with the same amounts of surface vacancies. For MnCo$_2$O$_4$-P, most surface metals occupy the octahedral sites while the MnCo$_2$O$_4$-A shows the higher concentration of tetrahedral site occupation on the surface. For all the geometry optimizations of the heterostructures, the following convergence criteria have been set including the Hellmann-Feynman forces should not exceed 0.001 eV/Å, and the total energy difference and the inter-ionic displacement should be less than $5 \times 10^{-5}$ eV/atom and 0.005 Å, respectively.

## Supporting Information

Supporting Information is available online from the Wiley Online Library or from the author.

**Conflict of Interest**

The authors declare no conflict of interest.

**Reference:**

[1] a) G. Yang, J. Zhu, P. Yuan, Y. Hu, G. Qu, B.-A. Lu, X. Xue, H. Yin, W. Cheng, J. Cheng, W. Xu, J. Li, J. Hu, S. Mu, J.-N. Zhang, *Nat. Commun.* **2021**, *12*, 1734; b) W. Xiang, N. Yang, X. Li, J. Linnemann, U. Hagemann, O. Ruediger, M. Heidelmann, T. Falk, M. Aramini, S. DeBeer, M. Muhler, K. Tschulik, T. Li, *Nat. Commun.* **2022**, *13*, 179.

[2] a) K. Dong, J. Liang, Y. Wang, Z. Xu, Q. Liu, Y. Luo, T. Li, L. Li, X. Shi, A. M. Asiri, Q. Li, D. Ma, X. Sun, *Angew. Chem. Int. Ed.* **2021**, *60,* 10583; b) Z. Shao, Q. Zhu, Y. Sun, Y. Zhang, Y. Jiang, S. Deng, W. Zhang, K. Huang, S. Feng, *Adv. Mater.* **2022**, DOI: 10.1002/adma.202110172.

[3] a) E. Jung, H. Shin, B.-H. Lee, V. Efremov, S. Lee, H. S. Lee, J. Kim, W. H. Antink, S. Park, K.-S. Lee, S.-P. Cho, J. S. Yoo, Y.-E. Sung, T. Hyeon, *Nat. Mater.* **2020**, *19*, 436. b) Y. Sun, L. Silvioli, N. R. Sahraie, W. Ju, J. Li, A. Zitolo, S. Li, A. Bagger, L. Arnarson, X. Wang, T. Moeller, D. Bernsmeier, J. Rossmeisl, F. Jaouen, P. Strasser, *J. Am. Chem. Soc.* **2019**, *141*, 12372.

[4] Y. Aoki, K. Takase, H. Kiuchi, D. Kowalski, Y. Sato, H. Toriumi, S. Kitano, H. Habazaki, *J. Am. Chem. Soc.* **2021**, *143*, 6505.

[5] C. Tang, L. Chen, H. Li, L. Li, Y. Jiao, Y. Zheng, H. Xu, K. Davey, S.-Z. Qiao, *J. Am. Chem. Soc.* **2021**, *143*, 7819.

[6] a) Y. Zhou, S. Sun, S. Xi, Y. Duan, T. Sritharan, Y. Du, Z. J. Xu, *Adv. Mater.* **2018**, *30*, 1705407; b) X. Xie, Y. Li, Z. Q. Liu, M. Haruta, W. Shen, *Nature* **2009**, *458*, 746.

[7] a) X. Ren, C. Wei, Y. Sun, X. Liu, F. Meng, X. Meng, S. Sun, S. Xi, Y. Du, Z. Bi, G. Shang, A. C. Fisher, L. Gu, Z. J. Xu, *Adv. Mater.* **2020**, *32*, 2001292; b) X. Ren, C. Wei, Y. Sun, X. Liu, F. Meng, X. Meng, S. Sun, S. Xi, Y. Du, Z. Bi, G. Shang, A. C. Fisher, L. Gu, Z. J. Xu, *Adv. Mater.* **2020**, *32*, 2001292.

[8] Y. Huang, A. Gomaa A. Mohamed, J. Xie, Y. Wang, *Nano Energy* **2021**, *82*, 105745.

[9] T. Ling, D.-Y. Yan, Y. Jiao, H. Wang, Y. Zheng, X. Zheng, J. Mao, X.-W. Du, Z. Hu, M. Jaroniec, S.-Z. Qiao, *Nat. Commun.* **2021**, *8*, 1509.

[10] a) P. P. Lopes, D. Y. Chung, X. Rui, H. Zheng, H. He, P. F. B. D. Martins, D. Strmcnik, V. R. Stamenkovic, P. Zapol, J. F. Mitchell, R. F. Klie, N. M. Markovic, *J. Am. Chem. Soc.* **2021**, *143*, 2741; b) P. P. Lopes, D. Y. Chung, X. Rui, H. Zheng, H. He, P. F. B. D. Martins, D. Strmcnik, V. R. Stamenkovic, P. Zapol, J. F. Mitchell, R. F. Klie, N. M. Markovic, *J. Am. Chem. Soc.* **2021**, *143*, 2741.

[11] Y. Duan, S. Sun, Y. Sun, S. Xi, X. Chi, Q. Zhang, X. Ren, J. Wang, S. J. H. Ong, Y. Du, L. Gu, A. Grimaud, Z. J. Xu, *Adv. Mater.* **2019**, *31*, 1807898.

[12] J. Liu, Q. Hu, Y. Wang, Z. Yang, X. Fan, L.-M. Liu, L. Guo, *PNAS* **2020**, *8*, 21906.

[13] J. Yin, Y. Li, F. Lv, Q. Fan, Y.-Q. Zhao, Q. Zhang, W. Wang, F. Cheng, P. Xi, S. Guo, *ACS Nano* **2017**, *11*, 2275.

[14] X. Zeng, J. Zhang, S. Zhu, X. Deng, H. Ma, J. Zhang, Q. Zhang, P. Li, D. Xue, N. J. Mellors, X. Zhang, Y. Peng, *Nanoscale* **2017**, *9*, 7493.

[15] C. Wei, Z. Feng, G. G. Scherer, J. Barber, Y. Shao-Horn, Z. J. Xu, *Adv. Mater.* **2017**, *29*, 1606800.

[16] a) M. Saruyama, Y.-G. So, K. Kimoto, S. Taguchi, Y. Kanemitsu, T. Teranishi, *J. Am. Chem. Soc.* **2011**, *133*, 17598; b) X. Zeng, J. Zhang, M. Si, D. Cao, X. Deng, H. M, Q. Lan, D. Xue, X. Zhang, K. Tao, Y. Peng, *Nanoscale* **2019**, *11*, 4385.

[17] Y. Ge, X. Qin, A. Li, Y. Deng, L. Lin, M. Zhang, Q. Yu, S. Li, M. Peng, Y. Xu, X. Zhao, M. Xu, W. Zhou, S. Yao, D. Ma, *J. Am. Chem. Soc.* **2021**, *143*, 628.

[18] a) L. An, B. Huang, Y. Zhang, R. Wang, N. Zhang, T. Dai, P. Xi, C.-H. Yan, *Angew. Chem. Int. Ed.* **2019**, *58*, 9459; b) J. Jin, J. Yin, H. Liu, B. Huang, Y. Hu, H. Zhang, M. Sun, Y. Peng, P. Xi, C.-H. Yan, *Angew. Chem. Int. Ed.* **2021**, *60*, 14117.

[19] Y. Zhou, S. Sun, J. Song, S. Xi, B. Chen, Y. Du, A. C. Fisher, F. Cheng, X. Wang, H. Zhang, Z. J. Xu, *Adv. Mater.* **2018**, *30*, 1802912.

[20] H. Ze, X. Chen, X.-T. Wang, Y.-H. Wang, Q.-Q. Chen, J.-S. Lin, Y.-J. Zhang, X.-G. Zhang, Z.-Q. Tian, J.-F. Li, *J. Am. Chem. Soc.* **2021**, *143*, 1318.

[21] L. An, J. Feng, Y. Zhang, R. Wang, H. Liu, G.-C. Wang, F. Cheng, P. Xi, *Adv. Funct. Mater.* **2019**, *29*, 1805298.

[22] Z.-F. Huang, J. Song, Y. Du, S. Xi, S. Dou, J. M. V. Nsanzimana, C. Wang, Z. J. Xu, X. Wang, *Nat. Energy* **2019**, *4*, 329.

[23] G. Meng, W. Sun, A. A. Mon, X. Wu, L. Xia, A. Han, Y. Wang, Z. Zhuang, J. Liu, D. Wang, Y. Li, *Adv. Mater.* **2019**, *31*, 1903616.

[24] C. C. L. McCrory, S. Jung, J. C. Peters, T. F. Jaramillo, *J. Am. Chem. Soc.* **2013**, *135*, 16977.

[25] Y. Zhou, S. Sun, C. Wei, Y. Sun, P. Xi, Z. Feng, Z. J. Xu, *Adv. Mater.* **2019**, *31*, 1902509.

[26] T. Wu, S. Sun, J. Song, S. Xi, Y. Du, B. Chen, W. A. Sasangka, H. Liao, C. L. Gan, G. G. Scherer, L. Zeng, H. Wang, H. Li, A. Grimaud, Z. J. Xu, *Nat. Catal.* **2019**, *2*, 763.

[27] V. Sannasi, K. Subbian, *Ceram. Int.* **2020**, *46*, 15510.

[28] Y. Wen, P. Chen, L. Wang, S. Li, Z. Wang, J. Abed, X. Mao, Y. Min, C. T. Dinh, P. D. Luna, R. Huang, L. Zhang, L. Wang, L. Wang, R. J. Nielsen, H. Li, T. Zhuang, C. Ke, O. Voznyy, Y. Hu, Y. Li, W. A. Goddard III, B. Zhang, H. Peng, E. H. Sargent, *J. Am. Chem. Soc.* **2021**, *143*, 6482.

[29] Z. Feng, W. T. Hong, D. D. Fong, Y.-L. Lee, Y. Yacoby, D. Morgan, Y. Shao-Horn, *Acc. Chem. Res.* **2016**, *49*, 966.

[30] M. W. Kanan, J. Yano, Y. Surendranath, M. Dincă, V. K. Yachandra, D. G. Nocera, *J. Am. Chem. Soc.* **2010**, *132*, 13692.

[31] a) C. C. L. McCrory, S. Jung, I. M. Ferrer, S.M. Chatman, J. C. Peters, T. F. Jaramillo, *J. Am. Chem. Soc.* **2015**, *137*, 4347; b) S. Sun, H. Li, Z. J. Xu. *Joule* **2018**, *2*, 1024.

[32] J. Yan, Y. Wang, Y. Zhang, S. Xia, J. Yu, B. Ding, *Adv. Mater.* 2020, 2007525.

[33] C. Wei, R. R. Rao, J. Peng, B. Huang, I. E. L. Stephens, M. Risch, Z. J. Xu, Y. Shao-Horn, *Adv. Mater.* **2019**, *31*, 1806296.

[34] J. Yin, J. Jin, M. Lu, B. Huang, H. Zhang, Y. Peng, P. Xi, C.-H. Yan, *J. Am. Chem. Soc.* **2020**, *142*, 18378.

[35] Y. Xia, X. Zhao, C. Xia, Z.-Y. Wu, P. Zhu, J. Y. Kim, X. Bai, G. Gao, Y. Hu, J. Zhong, Y. Liu, H. Wang, *Nat. Commun.* **2021**, *12*, 4225.

[36] W. Li, S. Xue, S. Watzele, S. Hou, J. Fichtner, A. L. Semrau, L. Zhou, A. Welle, A. S. Bandarenka, R. A. Fischer, *Angew. Chem. Int. Ed.* **2020**, *59*, 5837.

[37] L. An, C. Wei, M. Lu, H. Liu, Y. Chen, G. G. Scherer, A. C. Fisher, P. Xi, Z. J. Xu, C.-H. Yan, *Adv. Mater.* **2021**, *33*, 2006328.

[38] Y. Du, J. Wang, L. Jiang, L. S. Borgna, Y. Wang, Y. Zheng, T. Hu, *Journal of synchrotron radiation* **2014**, *21*, 756.

[39] Y. Zhou, Y. Du, S. Xi, Z. J. Xu, *Electrocatalysis* **2018**, *9*, 287.

[40] L. An, Y. Li, M.Luo, J. Yin, Y.-Q. Zhao, C. Xu, F. Cheng, Y. Yang, P. Xi, S. Guo, *Adv. Funct. Mater.* **2017**, *27*, 1703779.

[41] C. Wei, R. R. Rao, J. Peng, B. Huang, I. E. L. Stephens, M. Risch, Z. J. Xu, Y. Shao-Horn, *Adv. Mater.* **2019**, *31*, 1806296.

[42] J. Scholz, M. Risch, K. A. Stoerzinger, G. Wartner, Y. Shao-Horn, C. Jooss, *J. Phys. Chem. C* **2016**, *120*, 27746.

[43] C. C. L. McCrory, S. Jung, J. C. Peters, T. F. Jaramillo, *J. Am. Chem. Soc.* **2013**, *135*, 16977.

[44] S. J. Clark, M. D. Segall, C. J. Pickard, P. J. Hasnip, M. J. Probert, K. Refson, M. C. Payne, *Zeitschrift Fur Kristallographie* **2005**, *220*, 567.

[45] J. P. Perdew, K. Burke, M. Ernzerhof. *Phys Rev Lett* **1996**, *77*, 3865.

[46] P. J. Hasnip, C. J. Pickard, *Comput Phys Commun* **2006**, *174*, 24.

[47] J. P. Perdew, J. A. Chevary, S. H. Vosko, K. A. Jackson, M. R. Pederson, D. J. Singh, C. Fiolhais, *Physical Review B* **1992**, *46*, 6671.

[48] J. D. Head, M. C. Zerner, *Chem Phys Lett* **1985**, *122*, 264.